Geometric Binding Site Design for Surface-Tension Driven Self-Assembly

Xiaorong Xiong, Sheng-Hsiung Liang and Karl F. Böhringer

Department of Electrical Engineering University of Washington, Seattle, WA 98195-2500

Email: xrxiong@u.washington.edu

Abstract— **Surface-tension driven self-assembly techniques have been successfully employed to assemble and align micro parts on hydrophobic binding sites on a substrate. The driving force for assembly is provided by a liquid lubricant meniscus confined between two hydrophobic surfaces in an aqueous environment. Therefore, the hydrophobic pattern design becomes a critical issue for the self-assembly process. With an ideal design, the part can assemble in a unique position and orientation. In this paper, we study a series of geometric designs based on a first-order approximation energy model. An optimization method is developed to evaluate them, and a class of optimal designs is found consisting of asymmetric rings with additional geometric constraints.**

Keywords— **Self-assembly, micro assembly, MEMS, hydrophobic, hydrophilic, surface energy, surface tension force, binding site design.**
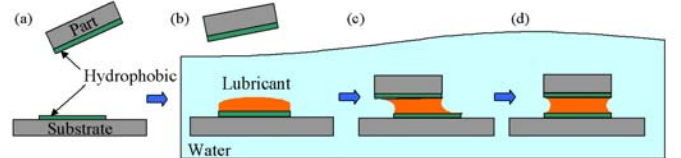
Fig. 1. Schematic plots of self-assembly flow. (a) The part and the substrate are patterned with hydrophobic binding sites. (b) The substrate with lubricant is immersed in water, and the lubricant wets exclusively the hydrophobic binding sites. (c) When the part is introduced in water and touches the lubricant, the lubricant will help assemble the part to the binding site on the substrate till (d) perfectly aligned.

I. INTRODUCTION

Advances in the areas of microelectromechanical systems (MEMS), materials and chemistry have enabled fabrication of a large variety of functional micro and even nano components. Micro system integration of different functionalities has emerged as a crucial problem, as they may be produced from different incompatible processes. A number of methods have been investigated to assemble micro and nano components: using the "pick-and-place" method [1–3]; using electrostatic force to drive assembly [4,5]; using aligned wafers to transfer microstructures [6,7]; using fluidic flow to assemble micro components into matching complementary trenches in a substrate [8]; using surface-tension force to self-assemble micro components into specially treated binding sites on a single substrate [9–14]. Surface-tension driven self-assembly has demonstrated the capability to assemble micro components with high efficiency and accuracy. Fig. 1 illustrates the schematic flow of this self-assembly technique. First, hydrophobic surfaces, which act as active binding sites, are patterned on hydrophilic background on a substrate (Fig. 1(a)). A hydrocarbon oil or melted solder lubricant, which is applied to the substrate, wets exclusively the hydrophobic binding sites in water (Fig. 1(b)). Micro components with matching hydrophobic patterns are then added to the water, self-assembled and aligned on the lubricant-wetted binding sites (Figs. 1(c)(d)). As the binding site geometries control the hydrocarbon shapes and therefore affect the assembly results, the geometric design is important for achieving good alignment. So far, most self-assembly experiments have been performed only with devices of symmetric binding sites with no preference in orientation, e.g. unpackaged square GaAs/GaAlAs LEDs and hexagonal mirrors [11, 12, 14]. Such devices can be aligned in multiple orientations: four for squares and six for hexagons. However, most other micro devices require a *unique* alignment position and orientation. For example, assembly of a packaged commercial LED requires a unique alignment in both orientation and position [13]. Therefore, an ideal geometric design should produce unique alignment, regardless of the initial pose of the part. From an energy point of view, the unique alignment corresponds to a global surface energy minimum without any other local minima for all configurations. A design satisfying this condition will be referred to as optimal in the following text.

To find the optimal designs, we discuss a constructive method. First, we introduce a first-order approximation model of the interfacial energy. Based on the model, we can calculate the surface energy, the driving forces or torques for assembly. A series of geometric designs including disks, symmetric rings and asymmetric rings with nonconcentric inner cutout are studied. From the energy and force (torque) analysis, a constructive optimization method is used to find optimal binding site shapes. As a result, symmetric ring shapes ensuring unique alignment position, and asymmetric rings ensuring unique alignment position and orientation, are obtained.

II. FIRST-ORDER APPROXIMATION MODEL OF SURFACE ENERGY

In this section, we introduce a first order approximation model for calculating the surface energy. Due to its computational simplicity, this method is preferable, e.g. compared to a three-dimensional finite element method (FEM) [15,16]

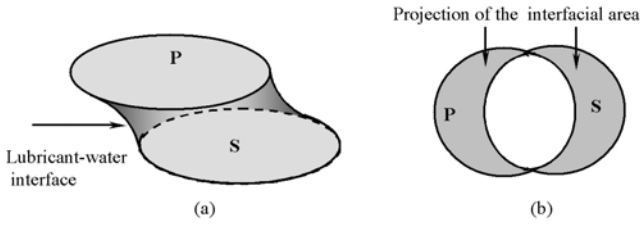using a software package called *Surface Evolver* [17]. A

Fig. 2. (a) Side view of the lubricant-water interfacial area. (b) The projection of the interfacial area to the substrate plane is shown as the shaded area. Note the lubricant thickness has been exaggerated.

brief derivation of the model is described as follows. With the assumption that shift between the part (P) and the substrate binding site (S) is much larger than the lubricant thickness, the water-lubricant interfacial area (Fig. 2(a)) can be approximated by its projection to the substrate plane shown as shaded areas in Fig. 2(b). Due to the linear relationship between the interfacial energy and area, we can approximate the interfacial energy E by the projection area (Fig. 2(b)):

$$E = \sigma(\mid S \mid + \mid P \mid -2 \mid S \cap P \mid) \tag{1}$$

where $\mid P \mid$, $\mid S \mid$ and $\mid S \cap P \mid$ denote the part, the substrate binding site and their overlap areas respectively, and σ is the lubricant-water interfacial tension.

Simulation results from the two different methods for a 500μm disk and a 1×1 mm^2 square are shown in Figs. 3 and 4. The first order approximation results are in good accordance with those from the three-dimensional FEM (*Surface Evolver*). Therefore, the projected area is a good approximation for the interfacial area, if the lubricant thickness is small compared to the binding site lateral size. Further-
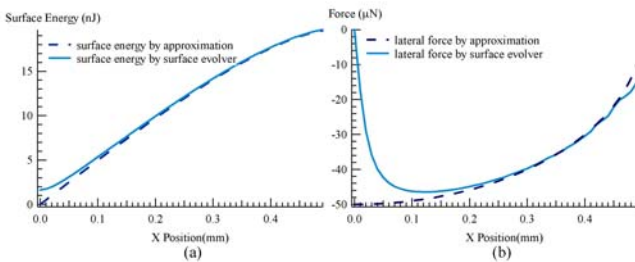

Fig. 3. Simulation results from the approximation model and *Surface Evolver* for 500μm circular binding site: (a) surface energy and (b) lateral surface tension force. Here we use σ=50mJ/m^2 and the lubricant volume is 0.0041mm^3.

more, since $\mid S \mid$ and $\mid P \mid$ in Eq. 1 are constant, the energy E depends exclusively on the overlap area $\mid S \cap P \mid$ and E is linear with $-\sigma \mid S \cap P \mid$ [18,19]. For simplicity, we calculate and analyze the overlap area instead of the surface energy in the rest of the paper. Therefore, the condition for an optimal design is that it has a unique overlap maximum in all the configurations.
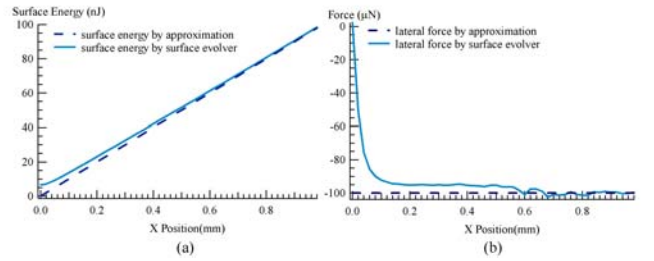

Fig. 4. Simulation results from the approximation model and *Surface Evolver* for 1×1mm^2 square binding site: (a) Surface energy and (b) lateral surface tension force. Here we use σ=50mJ/m^2 and the lubricant volume is 0.033mm^3.

In previous research [13, 19], different methods for binding site design have been discussed: design for a given site; design by exhaustive search; design by probabilistic approach; design via Fourier transform. In this paper, we discuss a new design method by using composite geometric shapes, formed by addition or subtraction of simple shapes such as disk, square, triangle, etc. Binding sites with simple geometry usually have more than one overlap area maximum. For example, square shapes have four overlap area maxima every 90°; circular shapes are rotationally symmetric, and have a unique overlap maximum in position but no preference in orientation. However, addition or subtraction of such shapes will break the symmetry. A simple example is a ring shape, which is the subtraction of two circular shapes of different sizes. If two circular shapes are not concentric, the ring shape might have a unique maximum in both position and orientation. Compared to the previous methods, this method is simple and easy to implement, however we cannot find all the possible optimal shapes by using this method.

In the following sections, we will focus on the composite shape design method. Particulary, composite patterns consisting of circular shapes of different sizes are used to create optimal designs.

III. BASIC GEOMETRIC ANALYSIS OF BINDING SITE DESIGNS

In this section, we introduce basic definitions and operations for pattern analysis. First, we introduce some terminologies that will be consistently used in the paper:

• Position (b, θ) denotes where the part is in a polar coordinate system.
• Orientation (γ) is the angular difference of a part with respect to a reference frame.
• Pose (b, θ, γ) denotes both the position and orientation.
• Position alignment $(\Delta b, \Delta \theta)$ is the relative position of a part to a binding site.
• Orientation alignment $(\Delta \gamma)$ is the relative orientation of a part to a binding site.
• Alignment $(\Delta b, \Delta \theta, \Delta \gamma)$ is the relative pose of a part to a binding site.

For convenience, we use the substrate binding site center as the origin. Therefore, the pose of the part and its alignment have the same value (b, θ, γ). For pattern analysis, we generate overlap area profiles. Each profile assigns an overlap area value to each part pose specified by (b, θ, γ). Similarly, overlap area derivative profiles are generated in terms of b, θ, γ respectively, which correspond to different driving force and torque profiles. We can evaluate these profiles and search for the optimal designs which ensure a unique maximum in overlap area.

For simplicity, we start with disks, for which the intersection area depends exclusively on the disk center distance. Then we study symmetric ring overlap area profiles, which can be derived in closed-form directly from overlap areas. With the analytical results from the disks and symmetric rings, we further our study to asymmetric rings in order to find the optimal patterns. From the results of such a series of shapes, we can derive some general design rules for the construction of optimal shapes.

A. Basic shapes

Definition 1: Disk: a disk shape is defined as $D(c, r)$ with center c and radius r.

Definition 2: Ring: a generalized ring is defined as $R(D_b, D_s)$ with outer bigger disk D_b and inner circular cutout D_s.

The parameters for generalized rings (Fig. 5) include (r_b, r_s, a), with r_b and r_s as the radii of D_b and D_s respectively and the offset $a = \parallel c_b - c_s \parallel$ as the distance between the disk centers. As the small disk has to be included in the large one, the condition $r_b \geq r_s + a$ must be satisfied. When offset $a = 0$, i.e. $c_b = c_s$, the rings are
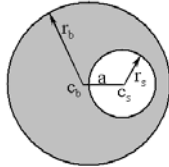

Fig. 5. The parameters of a generalized ring shape.

referred to as symmetric rings. Otherwise they are called asymmetric rings.

B. Disk-disk overlap area and its derivatives

Definition 3: Overlap area $A(P_1, P_2)$ denotes the intersection area between two different geometric shapes P_1 and P_2.

When the two patterns are disks (D_1 and D_2), the intersection area between them depends only on the distance $b = \parallel c_1 - c_2 \parallel$ between their centers. As shown in Fig. 6, the overlap area is the shaded area, which is the addition of two lens-shapes. Suppose the two circular shapes are D_1 and D_2 with their radii of r_1 and r_2 respectively. The intersection area can be calculated as:
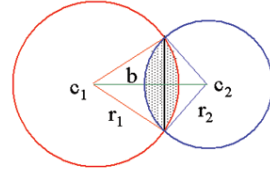

Fig. 6. The overlap area between two disks.

Proposition 1:

$$
A(D_1, D_2) = \begin{cases} 0, & \text{for} \quad b \geq r_1 + r_2 \\ -\dfrac{\sqrt{(-b+r_1+r_2)(b+r_1-r_2)(b-r_1+r_2)(b+r_1+r_2)}}{2} \\ +r_1^2 \arccos(\frac{b^2+r_1^2-r_2^2}{2br_1}) + r_2^2 \arccos(\frac{b^2+r_2^2-r_1^2}{2br_2}), \\ \text{for} \quad \mid r_1 - r_2 \mid < b < r_1 + r_2 \\ \min(\pi r_1^2, \pi r_2^2), & \text{for} \quad 0 \leq b \leq \mid r_1 - r_2 \mid \end{cases}
$$

$$(2)$$

Definition 4: $F(P_1, P_2)$ denotes the derivative of overlap area of two patterns P_1 and P_2 in terms of b.

When the two patterns are disks (D_1, D_2), it can be calculated as:

Corollary 1:

$$
F(D_1, D_2) = \frac{dA(D_1, D_2)}{db}
$$
$$
= \begin{cases} -\dfrac{\sqrt{(-b+r_1+r_2)(b+r_1-r_2)(b-r_1+r_2)(b+r_1+r_2)}}{b}, \\ \text{for} \quad \mid r_1 - r_2 \mid < b < r_1 + r_2 \\ 0, \quad \text{otherwise} \end{cases}
$$

$$(3)$$

The derivative $F(D_1, D_2)$ is basically the length of the intersecting segment between two disks.

When two disks D_1 and D_2 are of same size, i.e. $r_1 = r_2 = r$, the overlap area and its derivative are as follows:

Corollary 2:

$$
A(D_1, D_2) = \begin{cases} -\frac{b}{2}\sqrt{4r^2 - b^2} + 2r^2 \arccos(\frac{b}{2r}), \\ \text{for} \quad 0 \leq b < 2r \\ 0, \quad \text{for} \quad b \geq 2r \end{cases}
$$

$$(4)$$

Corollary 3:

$$
F(D_1, D_2) = \begin{cases} -\sqrt{4r^2 - b^2}, & \text{for} \quad 0 < b < 2r \\ 0, & \text{otherwise} \end{cases}
$$

$$(5)$$

C. Ring-ring overlap area and its derivatives

Suppose the two generalized rings $R_1(D_{1b}, D_{1s})$ and $R_2(D_{2b}, D_{2s})$ are identical, i.e. $r_{1b} = r_{2b} = r_b$ and $r_{1s} = r_{2s} = r_s$. To describe the relative pose between them, we use a triplet: (b, θ, γ) in the polar coordinate system, shown in Fig. 7. Here, b is the magnitude of vector $\overrightarrow{c_{1b}c_{2b}}$ and θ is the polar angle of $\overrightarrow{c_{1b}c_{2b}}$ in the domain of $0 \leq \theta < 2\pi$. The relative orientation between the two rings is represented by γ, with $0 \leq \gamma < 2\pi$. The overlap area between them can be decomposed into four parts (Fig. 8) as follows:

$$
\begin{aligned} A(R_1, R_2) &= \mid R_1 \cap R_2 \mid \\ &= \mid D_{1b} \cap D_{2b} \mid + \mid D_{1s} \cap D_{2s} \mid \\ &\quad - \mid D_{1b} \cap D_{2s} \mid - \mid D_{1s} \cap D_{2b} \mid \end{aligned}
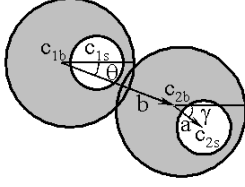$$

$$(6)$$

Fig. 7. The parameters to describe the intersection between two identical rings $R_1(D_{1b}, D_{1s})$ and $R_2(D_{2b}, D_{2s})$.

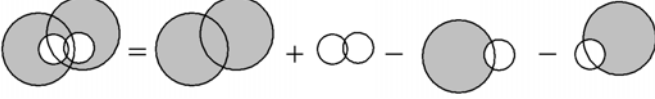It can be calculated from four disk-disk intersection areas:

Fig. 8. The intersection between two identical rings can be decomposed into four different disk-disk intersections.

Proposition 2:

$$A(R_1, R_2) = A(D_{1b}, D_{2b}) + A(D_{1s}, D_{2s})$$
$$- A(D_{1b}, D_{2s}) - A(D_{1s}, D_{2b}) \quad (7)$$

Since the overlap area of two disks only depends on their distance, the distances (Figs. 9(a)-(d)) between different circular shapes are calculated to find the overlap area:
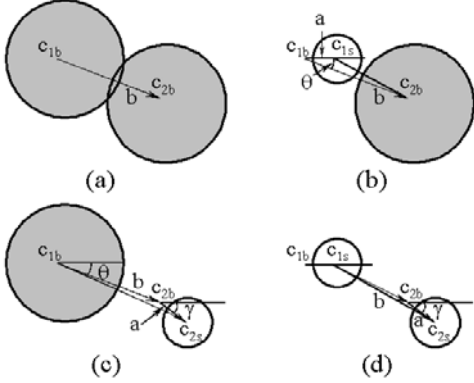

Fig. 9. The four components of the ring-ring overlap areas are intersections between different circular shapes with centers of c_{1b}, c_{2b}, c_{1s} and c_{2s} respectively. (a) Intersection between c_{1b} and c_{2b}. (b) The intersection between c_{1s} and c_{2b}. (c) The intersection between c_{1b} and c_{2s}. (d) The intersection between c_{1s} and c_{2s}.

$$\| c_{2b} - c_{1b} \| = b$$
$$\| c_{2b} - c_{1s} \| = \sqrt{a^2 + b^2 - 2ab\cos(\theta)}$$
$$\| c_{2s} - c_{1b} \| = \sqrt{a^2 + b^2 + 2ab\cos(\gamma - \theta)}$$
$$\| c_{2s} - c_{1s} \| =$$
$$\sqrt{(2a\sin(\gamma/2))^2 + b^2 - 4ab\sin(\gamma/2)\sin(\gamma/2 - \theta)} \quad (8)$$

$F_b(R_1, R_2)$, $F_\theta(R_1, R_2)$ and $F_\gamma(R_1, R_2)$ denote the derivatives of the overlap area between $R_1(D_{1b}, D_{1s})$ and $R_2(D_{2b}, D_{2s})$ in terms of b, θ and γ, respectively.

By substituting b's in Eq. 2, Eq. 4, Eq. 7 with the distances obtained in Eq. 8, we can express the overlap area in terms of (b, θ, γ). The first order derivatives in terms of b for each term in Eq. 7 can be simply derived as:

Proposition 3:

$$F_b(R_1, R_2) = F_{D_{1b}D_{2b}b} + F_{D_{1s}D_{2s}b} - F_{D_{1b}D_{2s}b} - F_{D_{1s}D_{2b}b}$$
$$F_{D_{1b}D_{2b}b} = F(D_{1b}, D_{2b})$$
$$F_{D_{1s}D_{2b}b} = F(D_{1s}, D_{2b})\frac{d(\sqrt{a^2 + b^2 - 2ab\cos(\theta)})}{db}$$
$$F_{D_{1b}D_{2s}b} = F(D_{1b}, D_{2s})\frac{d(\sqrt{a^2 + b^2 + 2ab\cos(\gamma - \theta)})}{db}$$
$$F_{D_{1s}D_{2s}b} = F(D_{1s}, D_{2s})$$
$$\frac{d(\sqrt{(2a\sin(\gamma/2))^2 + b^2 - 4ab\sin(\gamma/2)\sin(\gamma/2 - \theta)})}{db} \quad (9)$$

The first order derivatives in terms of θ for each term in Eq. 7 are:

$$F_\theta(R_1, R_2) = F_{D_{1b}D_{2b}\theta} + F_{D_{1s}D_{2s}\theta} - F_{D_{1b}D_{2s}\theta} - F_{D_{1s}D_{2b}\theta}$$
$$F_{D_{1b}D_{2b}\theta} = 0;$$
$$F_{D_{1s}D_{2b}\theta} = F(D_{1s}, D_{2b})\frac{d(\sqrt{a^2 + b^2 - 2ab\cos(\theta)})}{d\theta};$$
$$F_{D_{1b}D_{2s}\theta} = F(D_{1b}, D_{2s})\frac{d(\sqrt{a^2 + b^2 + 2ab\cos(\gamma - \theta)})}{d\theta};$$
$$F_{D_{1s}D_{2s}\theta} = F(D_{1s}, D_{2s})$$
$$\frac{d(\sqrt{(2a\sin(\gamma/2))^2 + b^2 - 4ab\sin(\gamma/2)\sin(\gamma/2 - \theta)})}{d\theta} \quad (10)$$

The first order derivatives in terms of γ for each term in the Eq. 7 are:

$$F_\gamma(R_1, R_2) = F_{D_{1b}D_{2b}\gamma} + F_{D_{1s}D_{2b}\gamma} - F_{D_{1b}D_{2s}\gamma} - F_{D_{1s}D_{2s}\gamma}$$
$$F_{D_{1b}D_{2b}\gamma} = 0$$
$$F_{D_{1s}D_{2b}\gamma} = 0$$
$$F_{D_{1b}D_{2s}\gamma} = F(D_{1b}, D_{2s})\frac{d(\sqrt{a^2 + b^2 + 2ab\cos(\gamma - \theta)})}{d\gamma}$$
$$F_{D_{1s}D_{2s}\gamma} = F(D_{1s}, D_{2s})$$
$$\frac{d(\sqrt{(2a\sin(\gamma/2))^2 + b^2 - 4ab\sin(\gamma/2)\sin(\gamma/2 - \theta)})}{d\gamma} \quad (11)$$

With the geometric analysis of the ring-ring overlap area and its derivatives, we can establish geometric models to find optimized binding site designs.

IV. Optimal Ring Shape Design

In this section, we first derive the sufficient condition for optimal patterns. We then study symmetric ring shapes. As a result, optimal symmetric rings are found, which can ensure a unique global maximum in overlap area for all positions. However, symmetric rings have no preference in orientation. In order to achieve a unique alignment pose, asymmetric rings are studied. Two feasible solutions are

derived to satisfy the optimization condition, and correspondingly two classes of optimal asymmetric rings are obtained.

A. Optimization objective and condition

As discussed above, an optimal pattern should allow only one energy minimum for all poses (b, θ, γ) between two geometric patterns. Therefore, the corresponding overlap area should have only one maximum. A sufficient condition for such designs is that regardless of the part's initial pose, there should exist a motion path, by following which the overlap area monotonically increases until the global maximum is reached. In the following sections, we discuss the possible paths satisfying this condition. To assure the existence of such paths, we derive the geometric constraints for different ring shapes including symmetric and asymmetric. Therefore, by finding the ring shapes satisfying the constraints, we can obtain a group of optimal rings.

B. Symmetric rings

With offset $a = 0$, the overlap area between two symmetric rings depends exclusively on their distance b, not θ or γ. Symmetric rings might have local maxima in overlap area [18] depending on the ratio r_s/r_b. Here, we analyze different ring configurations (r_s/r_b) based on our optimization model, and obtain quantitative results for optimized symmetric rings. Illustrations of the overlap area of $R_1(D_{1b}, D_{1s})$ and $R_2(D_{2b}, D_{2s})$ and its derivatives in terms of b are shown in Fig. 10. A sufficient condition for the ring
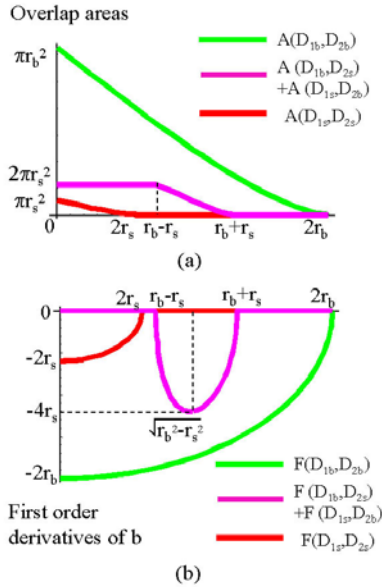

Fig. 10. (a) The overlap area profile between two identical symmetric rings $R_1(D_{1b}, D_{1s})$ and $R_2(D_{2b}, D_{2s})$. Different terms plotted in different colors denote the overlap areas of different disks. (b) The overlap area derivatives of with respect to b terms.

shape for having a unique maximum is

Theorem 1: The symmetric rings have unique overlap area maximum when the ratio between the inner disk radius and outer disk radius is no more than $\sqrt{\sqrt{108}/2 - 5}$.

The proof of this theorem is based on the sufficient condition that there must exist a continuous path, along which b decreases and overlap area increases. In other words, the derivative in terms of b: $F_b(R_1, R_2) = F(D_{1b}, D_{2b}) + F(D_{1s}, D_{2s}) - F(D_{1b}, D_{2s}) - F(D_{1s}, D_{2b})$, has to be no more than zero in the domain of $0 \leq b \leq 2r_b$. The different overlap area terms and their derivatives are shown in Fig. 10. From Fig. 10(b), we can see that $F(D_{1b}, D_{2s}) + F(D_{1s}, D_{2b})$ in the domains of $(0, r_b - r_s]$ and $[r_b + r_s, 2r_b)$ are zero. In addition, the maximum of the derivatives is in the domain of $[\sqrt{r_b^2 - r_s^2}, r_b + r_s)$. The sufficient condition is equivalent to that the derivative in the domain of $[\sqrt{r_b^2 - r_s^2}), r_b + r_s)$ has to be no more than zero:

$$F(D_{1b}, D_{2b}) - F(D_{1b}, D_{2s}) - F(D_{1s}, D_{2b})$$
$$= -\sqrt{4r_b^2 - b^2} +$$
$$\frac{2\sqrt{(-b + r_b + r_s)(b + r_b - r_s)(b - r_b + r_s)(b + r_b + r_s)}}{b}$$
$$\leq 0,$$
$$\text{for} \quad \sqrt{r_b^2 - r_s^2} \leq b < r_b + r_s \tag{12}$$

The solution to Eq. 12 is $r_s \leq \sqrt{\sqrt{108}/2 - 5}r_b$, with numerical approximation of $r_s \leq 0.442891r_b$. The rings satisfying this constraint will have a unique alignment position.

C. Asymmetric rings

For the asymmetric rings, the configurations include the ratios of r_s/r_b and a/r_b. With the inner cutout and outer disk not being concentric, both the orientation parameters θ and γ have to be considered for analysis. A parametric overlap derivative profile $(\gamma = \pi)$ in terms of b and θ is shown in Fig. 11. From the profiles, we can see there exists
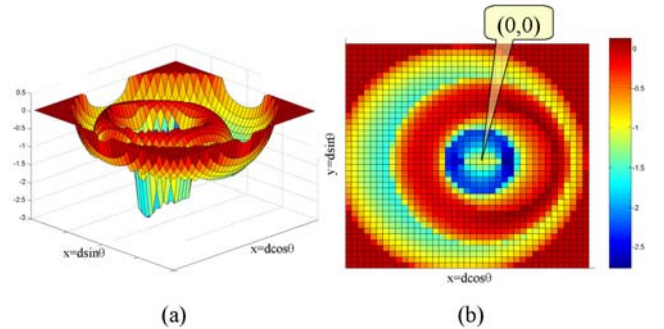

Fig. 11. An example of the overlap derivative profile for asymmetric ring shape. (a) Three-dimensional plot. (b) Intensity plot with color representing the derivative values.

a maximum derivative for any given (θ, γ). Such maxima

decrease from $\theta = 0$ to $\theta = \pi$ at $\gamma = \pi$ (Fig. 11(b)). From Eqs. 8 and 9, we can derive their lower bound at ($\theta = \pi$, $\gamma = \pi$) and upper bound at ($\theta = 0$, $\gamma = \pi$). Therefore, we have:

Proposition 4: If the maximal derivative at ($\theta = 0, \gamma = \pi$) is smaller than zero, all the derivatives are smaller than zero and the overlap function will have a unique global maximum.

Proposition 5: If the maximal derivative at ($\theta = \pi, \gamma = \pi$) is greater than zero, all the maxima at other orientations will be greater than zero and the overlap area will have local maxima.

With the sufficient condition for an optimal design: the existence of a motion path monotonically decreasing the overlap area, we construct two such motion paths from Proposition 4 and Proposition 5:

1. Motion path I (Fig. 12): translation and rotation. As illustrated in Fig. 12(a), one ring moves toward the center of the other until concentric, and during this movement the overlap area increases. Though two rings are concentric, they might not be aligned (Fig. 12(b)) and the ring will rotate until they are perfectly aligned (Fig. 12(c)) corresponding to maximum overlap area.
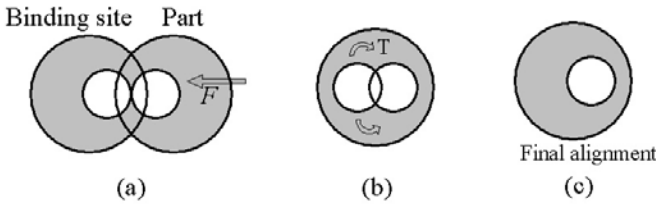

Fig. 12. Constructed path I. (a) The part approaches the fixed binding site with the derivative smaller than zero until their centers coincide. (b) The part then rotates till (c) perfect alignment.

2. Motion path II (Fig. 13): translation, rotation, translation and rotation. This motion path includes four different movements: first one ring translates toward the other until the overlap area no longer increases (Fig. 13(a)); the ring then rotates until the overlap area no longer increases (Fig. 13(b)); the next two movements are the same to those in motion path I, including translation and rotation shown in Figs. 13(c) and (d). Finally, the maximum overlap area is reached as shown in Fig. 13(e).

In summary, motion path I imposes stricter constraints on the rings, while motion path II is a less strict constraint for asymmetric rings to reach perfect alignment. The following sections are dedicated to analyze the different situations in order to find the solutions.

C.1 Motion path I

If paths in the motion path I category exist, they have to satisfy two conditions:
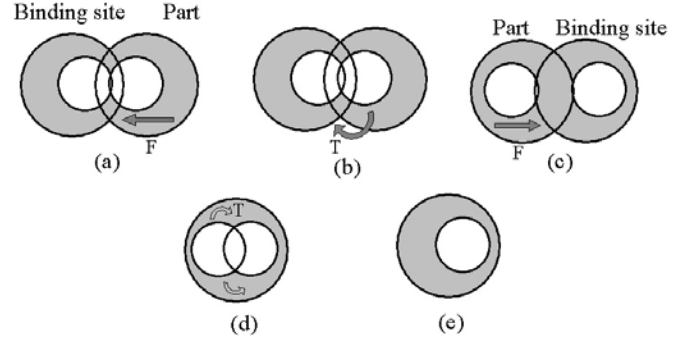1. There is only one overlap maximum at $b = 0$, regardless of the values of θ and γ.

Fig. 13. Constructed path II. (a) The part approaches the fixed binding site till the derivative is greater than zero. (b) The part then rotates along the center of the fixed binding site until the maximum overlap area is achieved. (c) The part then moves towards the center of the binding site till their centers coincides. (d) The part then rotates till (e) perfect alignment.

2. When $b = 0$, there is only one overlap maximum at $\gamma = 0$.

In order to satisfy the first condition of unique maximum at $b = 0$, the overlap derivatives in terms of b have to be non-negative for all possible θ and γ. From Proposition 4, such condition is satisfied when the derivatives are negative at ($\theta = 0$, $\gamma = \pi$) as shown in Fig. 12(a). The derivative consists of four different terms, illustrated
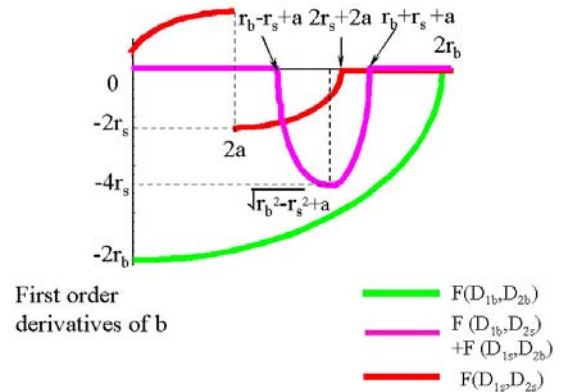

Fig. 14. The four terms of the first order overlap area derivative with respect to b.

in Fig. 14. From similar arguments in the symmetric ring section, we can derive the following inequality in the domain of $\sqrt{r_b^2 - r_s^2 + a} < b < r_b + r_s + a$:

$$-\sqrt{4r_b^2 - b^2} - \sqrt{4r_s^2 - (b - 2a)^2}$$
$$+\frac{2\sqrt{(a - b + r_b + r_s)(b - a + r_b - r_s)}}{b}$$
$$\times \sqrt{(b - a - r_b + r_s)(b - a + r_b + r_s)} \leq 0,$$
$$\text{when } \sqrt{r_b^2 - r_s^2 + a} < b < r_b + r_s + a \qquad (13)$$

Numerical solutions are obtained to Ineq. 13 and shown in Fig. 15(a). Each point in the plot of Fig. 15(a) is the solution to Ineq. 13, with the horizontal axis denoting the ratio of r_s/r_b and vertical axis of a/r_b .

From the second condition, we have that the first derivative of γ is non-positive, when $b = 0$ and the rotation angle γ is in the range of $[0, \pi]$ (Fig. 12(c)).

$$F_{D_{1s}D_{2s}\gamma} - F_{D_{1b}D_{2s}\gamma} \leq 0, \text{ when } b = 0, \theta = 0 \text{ and } 0 \leq \gamma \leq \pi.$$

From Eq. 11, we have

$$F_{D_{1s}D_{2s}\gamma} = -\sqrt{4r_s^2 - 4a^2 \sin(\gamma/2)^2} a \cos(\gamma/2)$$
when $b = 0$, $\theta = 0$ and $0 \leq \gamma \leq \pi$. (14)

$$F_{D_{1b}D_{2s}\gamma} = F(D_{1b}, D_{2s}) \frac{d(\sqrt{a^2 + b^2 + 2ab \cos(\gamma - \theta)})}{d\gamma} = 0,$$
when $b = 0$, $\theta = 0$ (15)

Therefore, Ineq. 14 can be simplified as

$$F_{D_{1s}D_{2s}\gamma} = -\sqrt{4r_s^2 - 4a^2 \sin(\gamma/2)^2} a \cos(\gamma/2) \leq 0,$$
when $b = 0$, $\theta = 0$ and $0 \leq \gamma \leq \pi$. (16)

The solution to Ineq. 16 is
$4r_s^2 - 4a^2 \sin(\gamma/2)^2 \geq 0$, as $a \cos(\gamma/2) \geq 0$, when $0 \leq \gamma \leq \pi$.
Therefore we have $a \leq r_s$, which means the inner circular cutout must include the center of the large circle. By combining both of the solutions for the translation and rotation conditions, we have the solutions as plotted in Fig. 15(b).
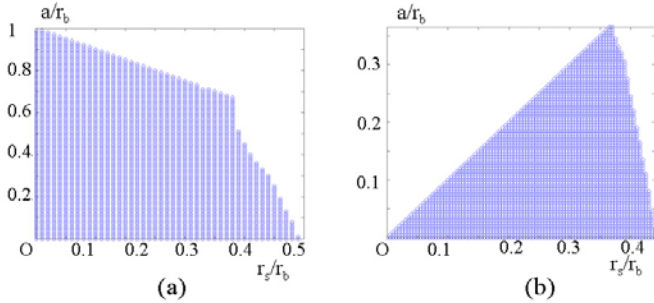

Fig. 15. Numerical solutions satisfying two constraints of motion path I. (a) Solutions to the first condition. (b) Solutions to both of the conditions.

In addition, we evaluate each feasible solution (r_s, a) by calculating the maximal derivative $F_{bmax}(R_1, R_2)$ for all feasible b in the domain of $(\sqrt{r_b^2 - r_s^2} + a, r_b + r_s + a)$. As in Fig. 16, each point in the surface represents a triplet $(r_s/r_b, a/r_b, F_{bmax}(R_1, R_2))$ with the feasible solution of $(r_s/r_b, a/r_b)$ and the corresponding maximum derivative value of $F_{bmax}(R_1, R_2)$ with $r_b = 1$.

C.2 Motion path II

In this section, we analyze paths in the motion path II category, which include four different movements. This
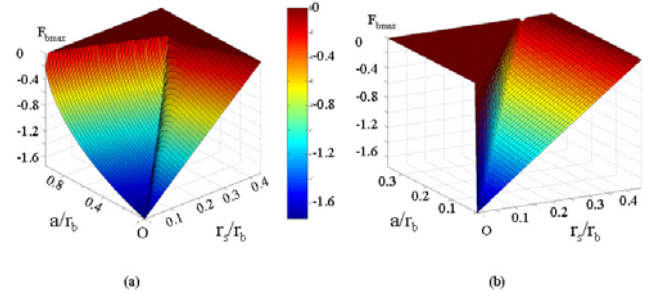

Fig. 16. Evaluations of solutions to motion path I. The function value corresponding to each point $(r_s/r_b, a/r_b)$ is the maximal overlap area derivative with respect to b in its domain of $(\sqrt{r_b^2 - r_s^2} + a, r_b + r_s + a)$. (a) Solutions to the first condition. (b) Solutions to both of the conditions.

path is derived from Proposition 5: the lower bound of the maximal derivatives at $(\theta = \pi, \gamma = \pi)$ has to be smaller than zero. Otherwise, there is no translation path that leads toward the binding site center and local maxima in overlap exist.

As illustrated in Figs. 13(a) and (b), the part can always reach the position shown in Fig. 13(c), as the overlap area reaches its maximum in terms of θ and γ. Therefore, to achieve the final perfect alignment, the overlap area must keep increasing during the movements illustrated in Fig. 13(c) and (d), which leads to two constraints:
1. The first order derivative of b is negative, when the part approaches from the thickest edge of the ring (Fig. 13(c)).

$$F_{D_{1b}D_{2b}b} + F_{D_{1s}D_{2s}d} - F_{D_{1b}D_{2s}b} - D_{1s}D_{2b}b \leq 0 \quad (17)$$

2. When $b = 0$, there is only one overlap maximum at $\gamma = 0$ (Fig. 13(d)). This condition is exactly the same as the second condition in Path I, with the solution to it as $a \leq r_s$.

The numerical solution of $(r_s/r_b, a/r_b)$ for the first condition is shown in Fig. 17(a). By combining both of the solutions to the translation and rotation conditions, we have the solutions as plotted in Fig. 17(b).
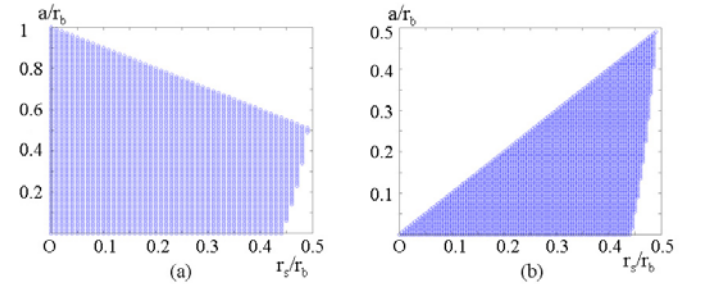

Fig. 17. Numerical solutions to motion path II. (a) Solutions to the first condition. (b) Solutions to both of the conditions.

In addition, we evaluate each feasible solution $r_s/r_b, a/r_b$, by calculating the maximal derivative $F_{bmax}(R_1, R_2)$ for all feasible b in the domain of $(\sqrt{r_b^2 - r_s^2} - a, r_b + r_s - a)$.
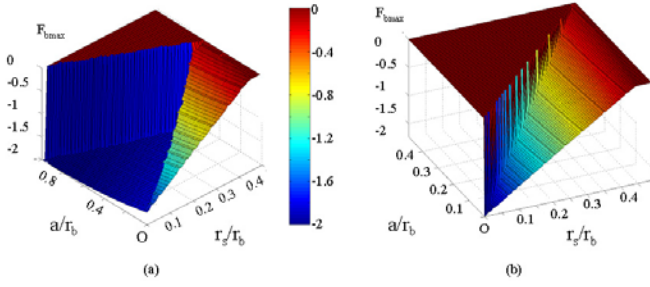
Fig. 18. Evaluations of solutions to motion path II. The function value corresponding to each point $(r_s/r_b, a/r_b)$ is the maximal overlap area derivative with respect to b in its domain of $(\sqrt{r_b^2 - r_s^2} - a, r_b + r_s - a)$. (a) Solutions to the first condition. (b) Solutions to both of the conditions.

As in Fig. 18, each point in the surface represents a feasible solution pair of $(r_s/r_b, a/r_b)$ with the evaluation value of $F_{bmax}(R_1, R_2)$.

By comparing solutions to motion path I and II, we observe the solutions to path II actually include those of path I due to the fact that the constraints on path I is stricter than those on path II.

V. Summary and conclusions

In this paper, we have discussed an optimization model of binding site design for surface-tension driven self-assembly techniques. We use a first order approximation model to simulate the surface energy by calculating overlap area. Based on the simulation results, we investigate a method to find optimal geometric shapes for alignment by using composite shapes. An analytical model is derived for simple composite shapes: rings. By using a constructive optimization method, we can decide the configurations of the rings in order to achieve unique alignment results.

From the results of optimizations, we have:

• Symmetric rings with the constraint $r_s \leq 0.442891 r_b$ achieve perfect alignment.

• We can generalize this results for symmetric rings. Any disk with a cutout pattern that can be enclosed in a circle with radius $r \leq 0.442891 r_b$, with r_b as the disk radius, can reach perfect alignment.

• Asymmetric rings that satisfy the constraints shown in Fig. 17 and Fig. 15 are optimal.

In practice, experiments are performed to test these designs [20], and accordant results have been obtained. In conclusion, these geometric binding site design methods have provided solutions to achieve unique alignment for self-assembly techniques. The results from this work will help us gain more general insights into this technique, with the intention to understand and optimize the self-assembly process and to improve the assembly yield for microsystem integration.

References

[1] S. J. Ralis, B. Vikramaditya, and B. J. Nelson, "Micropositioning of a weakly calibrated microassembly system using coarse-to-fine visual servoing strategies," *IEEE Transactions on Electronics Packaging Manufacturing*, vol. 23, no. 2, pp. 123 –131, 2000.
[2] G. Yang, J. A. Gaines, and B. J. Nelson, "A flexible experimental workcell for efficient and reliable wafer-level 3D microassembly," in *Proc. IEEE International Conference on Robotics and Automation (ICRA)*, Seoul, South Korea, 2001, pp. 133 –138.
[3] J. A. Thompson and R. S. Fearing, "Automating microassembly with ortho-tweezers and force sensing," in *Proc. IEEE/RSJ International Conference on Intelligent Robots and Systems (IROS)*, Maui, HI, 2001, pp. 1327 –1334.
[4] K. F. Böhringer, R. S. Fearing, and K. Y. Goldberg, "Microassembly," in *The Handbook of Industrial Robotics*, 2nd ed., S. Nof, Ed. John Wiley & Sons, February 1999, pp. 1045–1066.
[5] nanogen, "http://www.nanogen.com," Nanogen 10398 Pacific Center Ct. San Diego, CA 92121.
[6] M. B. Cohn, K. F. Böhringer, J. M. Noworolski, A. Singh, C. G. Keller, K. Y. Goldberg, and R. T. Howe, "Microassembly technologies for MEMS," in *Proc. SPIE Micromachining and Microfabrication*, Santa Clara, CA, 1998, pp. 2–16.
[7] A. S. Holmes and S. M. Saidam, "Sacrificial layer process with laser-driven release for batch assembly operations," *ASME/IEEE J. of Microelectromechanical Systems*, vol. 7, no. 4, pp. 416–422, 1998.
[8] H. J. Yeh and J. S. Smith, "Fluidic assembly for the integration of GaAs light-emitting diodes on si substrates," *IEEE Photonics Technology Letters*, vol. 46, pp. 706–709, 1994.
[9] A. Terfort, N. Bowden, and G. M. Whitesides, "Three-dimensional self-assembly of millimetre-scale components," *Nature*, vol. 386, pp. 162–164, 1997.
[10] D. Gracias, J. Tien, T. L. Breen, C. Hsu, and G. M. Whitesides, "Forming electrical networks in three dimensions by self-assembly," *Science*, vol. 289, pp. 1170–1172, 2000.
[11] U. Srinivasan, D. Liepmann, and R. T. Howe, "Microstructure to substrate self-assembly using capillary forces," *ASME/IEEE J. of Microelectromechanical Systems*, vol. 10, no. 1, pp. 17–24, 2001.
[12] H. O. Jacobs, A. R. Tao, A. Schwartz, D. H. Gracias, and G. M. Whitesides, "Fabrication of a cylindrical display by patterned assembly," *Science*, vol. 296, pp. 323–325, 2002.
[13] X. Xiong, Y. Hanein, W. Wang, D. T. Schwartz, and K. F. Böhringer, "Controlled multibatch self-assembly of microdevices," *Journal of Microelectromechanical Systems*, vol. 12, no. 2, pp. 117– 127, 2003.
[14] U. Srinivasan, M. H. Helmbrecht, C. Rembe, R. S. Muller, and R. T. Howe, "Fluidic self-assembly of micromirrors onto microactuators using capillary forces," *IEEE Journal on Selected Topics in Quantum Electronics*, vol. 8, no. 1, pp. 4–11, 2002.
[15] A. Greiner, J. Lienemann, J. G. Korvink, X. Xiong, Y. Hanein, and K. F. Böhringer, "Capillary forces in micro-fluidic self-assembly," in *Fifth International Conference on Modeling and Simulation of Microsystems (MSM'02)*, San Juan, Puerto Rico, USA, April 22-25, 2002.
[16] J. Lienemann, A. Greiner, J. G. Korvink, X. Xiong, Y. Hanein, and K. F. Böhringer, "Modelling, simulation and experimentation of a promising new packaging technology - parallel fluidic self-assembly of micro devices," *Sensors Update*, vol. 13, no. 1, pp. 3–43, December 2003.
[17] K. Brakke, "Surface evolver," Mathematics Department, Susquehanna University, Selinsgrove, PA, 1870-1001, 1999.
[18] K. F. Böhringer, U. Srinivasan, and R. T. Howe, "Modeling of capillary forces and binding sites for fluidic self-assembly," in *Proc. of IEEE Workshop on Micro Electro Mechanical Systems (MEMS)*, Switzerland, 2001, pp. 369–374.
[19] X. Xiong, Y. Hanein, W. Wang, D. T. Schwartz, and K. F. Böhringer, "Multi-batch micro-selfassembly via controlled capillary forces," in *Proc. IEEE/RSJ International Conference on Intelligent Robots and Systems (IROS)*, Maui, HI, 2001, pp. 1335 – 1342.
[20] S.-H. Liang, X. Xiong, and K. F. Böhringer, "Towards optimal designs for self-alignment in surface tension driven microassembly," in *17th IEEE International Conference on Micro Electro Mechanical Systems (MEMS)*, Maastricht, Netherlands, 2004.